Int. J. Electrochem. Sci., 16 **(2021)** Article Number: 211144, doi: 10.20964/2021.11.47

International Journal of
ELECTROCHEMICAL
SCIENCE
www.electrochemsci.org

Simulation and Experimental Investigation of Electrochemical Trepanning of an Aero-Engine Diffuser with Different Flow Fields

Zhouzhi Gu[1], *Xiaohu Zheng*[1*] , *Yongcheng Ge*[2]

[1] Jiangsu Key Laboratory of Advanced Manufacturing Technology, Huaiyin Institute of Technology , Huai'an 223000, China
[2] College of Mechanical Engineering, Yangzhou University, Yangzhou 225127, China
[*]E-mail: hyzxh@126.com

Received: 13 June 2021 / *Accepted:* 20 September 2021 / *Published:* 10 October 2021

The electrochemical-trepanning process is an economical approach for manufacturing diffuser structures. In the electrochemical-trepanning process, the flow field is an important factor that affects machining stability, machining efficiency, and surface quality. In this study, two different flow fields of the forward flow-field mode and the lateral flow-field mode were proposed, and their numerical models were also established and then simulated using FLUENT software. The results showed that the flow velocity of the forward flow-field mode was higher, and the flow velocity of the lateral flow-field mode was more uniform. Furthermore, a fixture was designed to realize this new flow mode, and then corresponding experiments were carried out. The experimental results illustrated that the forward flow-field mode could get a better feed speed of 2.5 mm/min, and the lateral flow-field mode could get a better surface quality of 1.581 μm. In addition, since the lateral flow field was more uniform, the flow pattern on the machined surface disappeared, and the machining quality was greatly improved.

Keywords: electrochemical machining; flow field; experiment; diffuser

1. INTRODUCTION

Diffusers are one of the key components of an aero-engine. They have the characteristics of a complex structure, thin-blade wall, and difficult cutting material, which bring great challenges to traditional machining technology [1]. Electrochemical machining (ECM) is one of the non-traditional machining techniques, with the advantages of no cutting force and no tool wear, regardless of material characteristics [2-3]. Therefore, electrochemical machining is regarded as a promising and low-cost process for yielding various components of difficult-to-machine materials and has been well established in diverse applications [4-5].

In the ECM process, the appropriate electrolyte flow field has a positive impact on the machining efficiency, machining accuracy, and surface roughness. At present, many studies have carried out in-depth research on the flow field in electrochemical machining [6]. Zhu et al. proposed a new centerline method to improve the machining efficiency and accuracy significantly. In addition, they also enhanced the blade accuracy by adding back pressure to the machining zone [7]. In the process of electrochemical machining, Xu et al. designed a p-type flow-field mode to improve the cathode feed rate and surface roughness [8]. Fang et al. proposed a pulse electrolyte-flow method, which enhanced the transfer effect of processing products, such as bubbles and heat transfer, and improved the profile accuracy of the anode surface [9]. Tang et al. analyzed the influence of the cathode structure on the flow field in the ECM gap and designed the optimized cathode structure to greatly improve the machining efficiency [10]. Ge et al. carried out research on deep electrochemical machining, obtained the optimized flow-field model through a simulation experiment, and greatly improved the machining efficiency in the experiment [11]. Paczkowski et al. constructed a mathematical model of two problems and discussed the distribution characteristics of the electrolyte flowrate, pressure, inter-electrode gap thickness, and other parameters [12]. Zaytsev et al. carried out research on jet electrochemical-machining technology and analyzed the influence of the cathode structure on the cavitation effect of the flow field [13].

In this paper, the different flow-field characteristics of the ECM of diffusers were studied. Two flow-field modes were designed, and the simulation experiments were carried out. Two kinds of fixtures with different flow-field modes were designed, and verification experiments were also carried out. Lastly, the influence of the two flow-field modes on the machining process was discussed.

2. DESCRIPTION OF FLOW-FIELD MODE

In electrochemical machining, the flow field is the key factor affecting the machining stability, machining efficiency, and surface quality. In order to improve the blade surface quality, two flow-field models were constructed, as shown in Figures 1 and 2.

Figure 1 shows the schematic diagram of forward flow for electrochemical trepanning. The sleeve cathode adopts a hollow-structure design, and the inner cavity of the electrode needs to be coated with an insulating layer. During processing, the cathode is fed downward at a certain speed, and the workpiece remains stationary. The electrolyte flows in from the cathode cavity, enters the end-surface machining gap from the front end of the cathode blade, and flows out from the outer gap along the side wall of the cathode.

Figure 2 shows the schematic diagram of lateral flow for electrochemical trepanning. The electrolyte flows in from the leading edge and out from the trailing edge, flowing uniformly along the y-direction. The vertical section of the lateral flow mode is shown in Figure 2(b). In this method, the blind-hole structure of the insulating water jacket is adopted, and the top of the water jacket is closed, which can weaken the electrolyte flow in the side gap. The gap outlets on both sides are equipped with sealing fixtures, which are compressed by springs to limit the electrolyte outflow from the gaps on both sides.

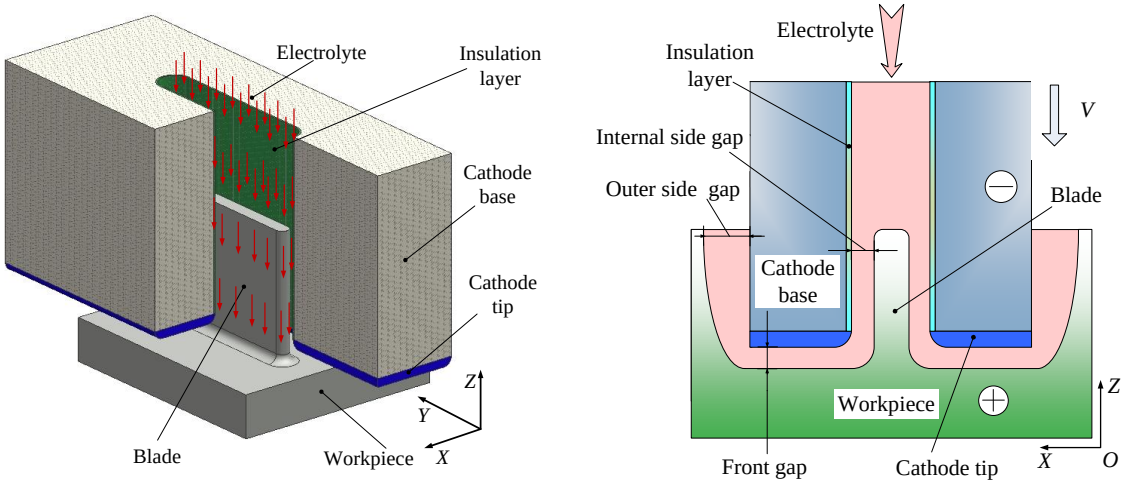

(a) Forward flow (b) Application of forward flow

Figure 1. Schematic diagram of forward flow for electrochemical trepanning.

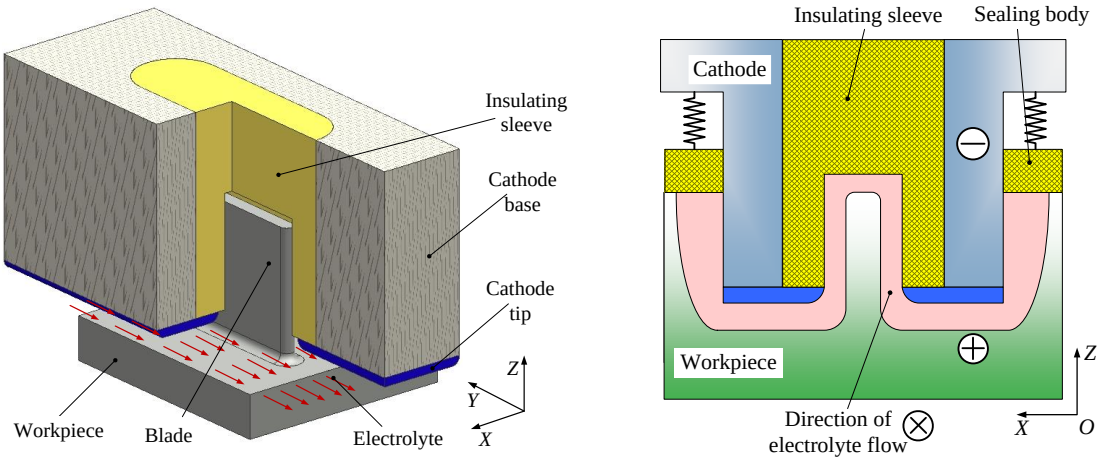

(a) Lateral flow (b) Application of lateral flow

Figure 2. Schematic diagram of lateral flow for electrochemical trepanning.

3. SIMULATION OF TREPANNING ECM

3.1 Theoretical model of the flow field

The flow field in electrochemical machining is a typical multiphase flow. In addition to the electrolyte, the flow field also contains gases, flocculent metal oxides, and heat products produced in the machining process. In order to simplify the simulation model, the flow field was assumed to be liquid single-phase flow, and the electrolyte fluid was assumed as follows.

1) The fluid was an incompressible fluid. During the simulation, the compressibility of the fluid was not considered, and the influence of the pressure and temperature of the flow field on the density and volume of the fluid was ignored.

2) The fluid was considered a Newtonian fluid, that is, the shear stress and shear strain of the fluid comply with Newton's law of internal friction.

3) There was no slip between the fluid and the boundary, that is, there was no relative motion at the interface between the liquid and the solid.

The core of different flow-field simulations is to determine the governing equation according to the fluid properties and flow state. The flow state is determined by Reynolds number Re, as shown below:

$$Re = \frac{uD_h}{\nu}, \qquad (1)$$

where u is the electrolyte velocity (according to experimental experience, the velocity budget value is 15 m/s), ν is the kinematic viscosity of the electrolyte (the actual calculated value is 0.805×10^{-6} m^2/s for water at 30°C), and D_h is the hydraulic diameter of the flow-channel section.

According to the abovementioned assumptions and the calculated value of the Reynolds number Re, it can be determined that the governing equation of the flow-field simulation is the incompressible Navier-Stokes equation based on the Reynolds average. The formula is as follows:

$$\frac{\partial \bar{u}_i}{\partial x_i} = 0 \qquad (2)$$

$$\frac{\partial \bar{u}_i}{\partial x_j} + \bar{u}_j \frac{\partial \bar{u}_i}{\partial x_j} = -\frac{\partial \bar{p}}{\partial x_i} + \nu \frac{\partial^2 \bar{u}_i}{\partial x_j \partial x_j} - \frac{\tau_{ij}}{\partial x_j}, \qquad (3)$$

where $\bar{u}_i$ is the i-direction component of the time-mean velocity, x_i is the i-direction coordinate of the coordinate system, x_j is the j-direction coordinate of the coordinate system, $\bar{p}$ is the time-mean pressure, and τ_{ij} is the component of the stress tensor in the ij-plane.

Based on the description in the second section of this paper, the geometric model of the fluid simulation was constructed as shown in Figures 3 and 4. In this case, Figure 3 shows the geometric model of forward flow, and Figure 4 shows the geometric model of lateral flow. In order to analyze the flow field distribution in the vertical section of the processing area and the flow channel, the monitoring surfaces P1 and P2 were designed in the flow-field geometry, as shown in Figures 3 and 4. The P1 plane was located between the leading edge and the trailing edge and was perpendicular to the hub of the blade. The P2 plane was located in the middle of the end clearance and was parallel to the straight blade hub. The boundary conditions of the calculation model are shown in Table 1.

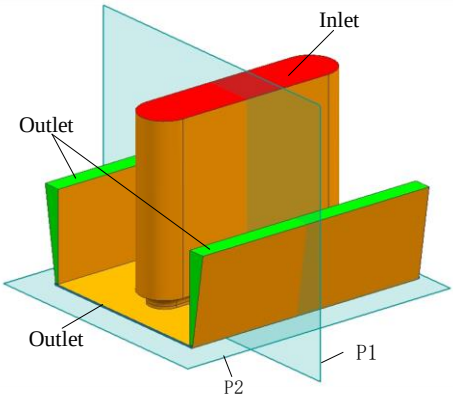

Figure 3. Boundary definition of forward flow.

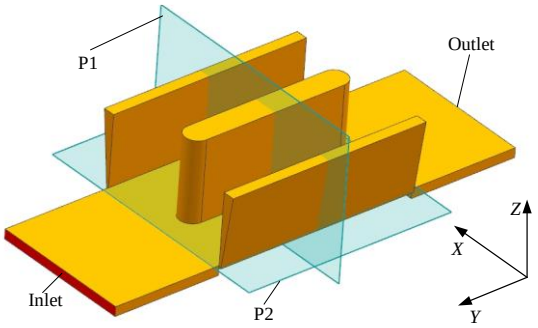

Figure 4. Boundary definition of lateral flow.

Table 1. Boundary conditions of flow-field simulation.

Boundary condition	Value
Inlet pressure	1.2 MPa
Outlet pressure	0 MPa
Wall velocity	0 and no slippage

3.2 Simulation and results

The pressure-distribution cloud diagram in the P1 plane (the vertical section of the flow passage) is shown in Figure 5. The velocity distribution in the vertical section of the orthoflow field is shown in Figure 5(a), and it can be seen from the figure that the flow velocity in the gap between the end face and the side face was relatively high. The velocity distribution in the vertical section of the side-stream field is shown in Figure 5(b), and it can be seen from the figure that the flowrate of electrolyte in the side clearance was generally low. The flowrate was high only near the end clearance, and the velocity in the end gap was significantly higher than that in the side gap, where the velocity distribution was between 20 m/s and 30 m/s. This showed that most of the electrolyte flowed through the processing zone, and the side gap had little effect on the electrolyte diversion.

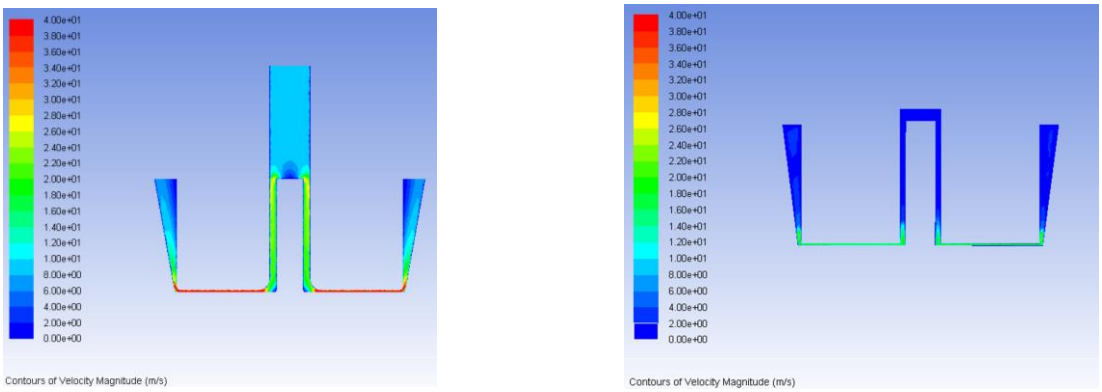

(a) Forward flow (b) Lateral flow

Figure 5. Contours of velocity magnitude at P1 of forward flow and lateral flow.

Figure 6 shows a quantitative analysis of the velocity distribution of P1 in the two flow-field modes; a monitoring line was set on the vertical section of the runner, as shown in Figure 6(a). One-hundred and fifty sampling points were evenly distributed on the monitoring line, and the velocity-change curve in the gap was drawn using the node data on the monitoring line (Figure 6(b)). In the side-flow mode, the flow velocity in the end gap was close to 25 m/s, and the flow velocity in the gap between the inner and outer sides was close to 0. In the forward-flow mode, the flow velocity in the end-face gap was close to 40 m/s, the flow velocity in the inner gap was close to 30 m/s, and the velocity in the outer gap showed a downward trend but was generally higher than 15 m/s. The flow velocity of the end-face gap in the side-flow mode was lower than in the forward-flow mode, which led to the decrease of the product-removal ability and affected the feeding rate of the side-flow sleeve. However, in the side-flow mode, the flow velocity of the side gap was extremely low, the electrolyte flow was effectively suppressed, and the processing products such as bubbles were easy to accumulate here, which helped to reduce the stray corrosion of the blade and improve the processing quality of the blade.

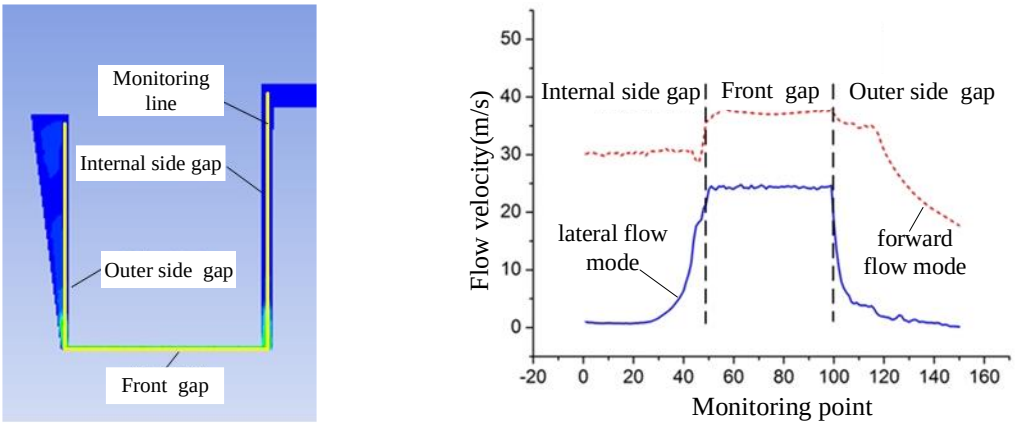

(a) Monitoring line (b) Velocity curve

Figure 6. Velocity distribution curve in the machining gap.

The pressure-distribution cloud diagram in the P2 plane (the horizontal section of the flow passage) is shown in Figure 7. The pressure cloud diagram of the orthoflow field is shown in Figure 7(a), along with the pressure nephogram of the orthoflow field. As can be seen in the figure, the electrolyte pressure near the blade body was relatively high, up to 1.2 MPa. However, due to the expansion of the flow-passage section, the pressure in the front and rear edges of the blade dropped sharply, which led to the expansion of the bubble volume. This resulted in the uneven dissolution of the hub surface and even short circuiting during the processing. Figure 7(b) shows the pressure nephogram of the side-stream field. It can be seen from the figure that the pressure gradient in the end gap of the side-stream field was small, and the pressure of the electrolyte dropped slowly from the inlet to the outlet. There was no local sudden change of pressure in the flow field to cause the accumulation of bubbles and other products, and therefore the processing stability was ensured.

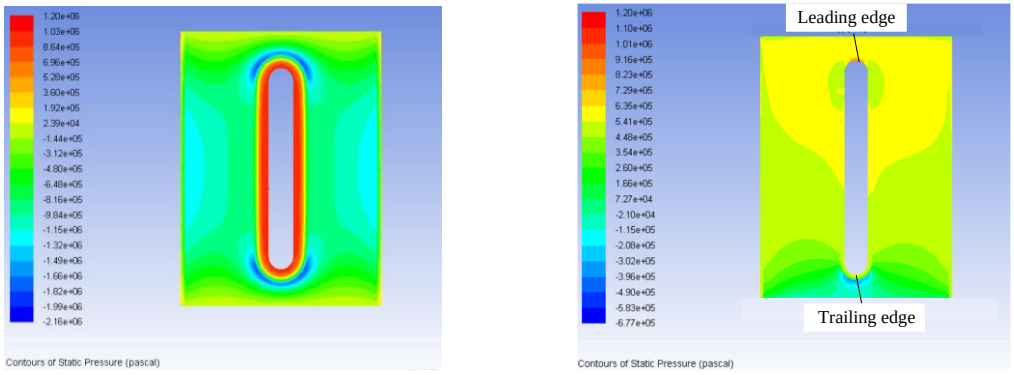

(a) Forward flow (b) Lateral flow

Figure 7. Contours of pressure at P2 of forward flow and lateral flow.

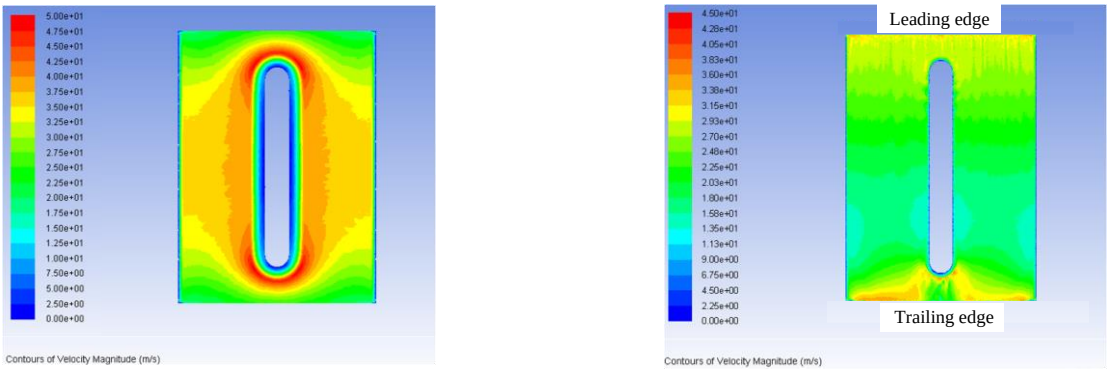

(a) Forward flow (b) Lateral flow

Figure 8. Contours of velocity magnitude in the end gap of forward flow and lateral flow.

The velocity-distribution cloud diagram in the P2 plane (the horizontal section of the flow passage) is shown in Figure 8. It can be seen from the velocity-vector diagrams of the two flow fields that the electrolyte flow in the processing zone of the orthoflow field was divergent, and the velocities on both sides of the blade were the highest at close to 50 m/s. Conversely, the electrolyte flow at the front and rear edges of the blade and the hub edge was low, at only about 20 m/s, and so the velocity difference was large. The electrolyte flowed in parallel in the processing area of the lateral flow field, and the flow velocity was uniform with an overall distribution of 17.5–29.5 m/s. In conclusion, from the comparison of the simulation results of the two flow fields, it was seen that the electrolyte flow was sufficient, and the velocity distribution was uniform in the machining area of the side-stream field. In addition, the electrolyte flow in the side gap of the side stream field was obviously restricted with a flowrate close to 0 m/s, which could weaken the stray current in the side gap and help to improve the surface quality of the machined blade.

4. EXPERIMENTAL RESULTS AND DISCUSSION

4.1. Experimental procedures

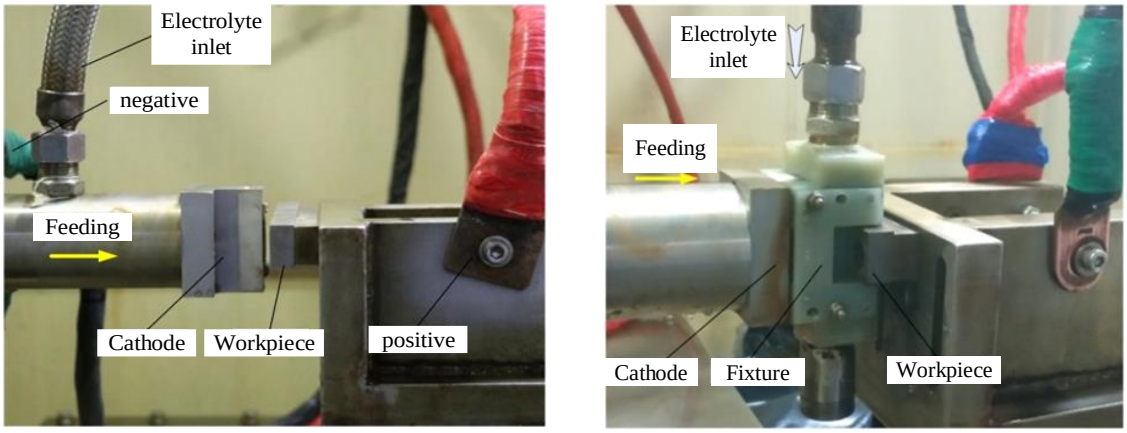

(a) Forward-flow fixture (b) Lateral-flow fixture

Figure 9. Machining equipment on site.

To verify the simulation process, two type fixtures for the forward-flow mode and lateral-flow mode were manufactured separately. The machining conditions are displayed in Table 2. The process sites of the forward-flow fixture and lateral-flow fixture are shown in Figures 9(a) and 9(b), respectively, and the non-processing areas were insulated. In order to ensure that the electrolyte provided by the inlet to the inter-electrode gap was always the same, during the processing the electrolyte inlet was fed along with the movement of the cathode. The machined samples were then measured: the roughness tester (MAHR PS1) was used to measure the surface roughness of the sample, and the coordinate-measuring machine (TESA Micro-Hite 3D) was used to test the machining accuracy.

Table 2. Conditions of the experiments.

name	numerical value
Processing voltage	DC 20 V
Electrolyte composition	20% $NaNO_3$
Electrolyte inlet pressure	1.2 MPa
Electrolyte temperature	30°C
Initial machining gap	0.5 mm
Workpiece material	GH 4169
Cathode feed rate	1, 1.5, 2, 2.5, 3 mm/min

4.2 Comparison of the feed rate of the cathode tool

Under the above-mentioned conditions, a series of experiments with different feed rates were carried out, and the machining current was collected and plotted, as shown in Figure 9.

Figure 10(a) shows the change curve of the machining current under forward flow. From the figure, when the machining speed was 0.5 mm/min, the current changed slowly in the machining process, mainly because of the low feed speed, which resulted in the end-face balance gap and the initial machining gap being approximately equal. When the feeding rate was 1–2.5 mm/min, in the initial stage of processing, when the end-face gap transitioned from the initial value to the equilibrium value, the current rose sharply. After the feed depth reached 1.5 mm, the current tended to be stable, indicating that the processing had entered the balance state. When the feeding rate was continuously increased to 3 mm/min, the processing process entered an unstable state, causing the processing current to fluctuate greatly and sparking to occur at any time.

Figure 10(b) shows the change curve of the machining current under lateral flow. From the figure, when the machining speed was 2 mm/min, current fluctuations occurred at the end of processing, mainly because the cathode feed speed was too high, resulting in a smaller end-face balance gap. Additionally, the processing products could not be discharged in time, which led to unstable processing. When continuing to increase the feeding rate to 2.5 mm/min, the processing process failed to proceed smoothly. Therefore, the limit for the machining speed of electrochemical machining in the lateral-flow mode was only 2 mm/min. Compared with the maximum machining speed of 2.5 mm/min in forward flow, the machining speed that could be achieved by lateral flow was slightly lower.

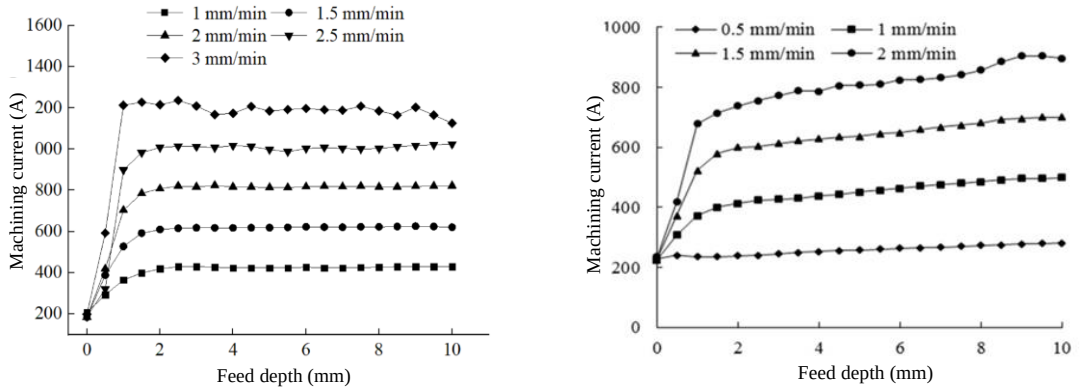

(a) Forward flow with different feeding rates (b) Lateral flow with different feeding rates

Figure 10. Current changes during the electrochemical trepanning of the blade process.

4.3 Comparison of surface topography of machined samples

To comprehensively evaluate the machining characteristics of forward flow and lateral flow, the surface quality of machined samples was analyzed under the same feed rate of 2 mm/min.

Figures 11 and 12 show the actual photos of the blade samples obtained using forward flow and lateral flow, respectively. It is clear from Figure 10 that the hub of the blade processed by the forward flow mode of electrochemical trepanning was not smooth, and there were irregular protrusions at the front and rear edges of the blade. It is obvious from the enlarged image (Figure 11(c)) taken by the optical microscope that there was serious pitting corrosion on the blade surface. Lateral flow was able to ensure

the uniform distribution of pressure and velocity in the end gap and improve the dissolution uniformity of the blade-hub surface, causing the hub machined by lateral flow to be smoother (Figures 12(a) and 12(b)). In addition, the lateral flow mode of electrochemical trepanning could reduce the electrolyte flowrate on the blade surface, make the processed products gather in the side gap, and then reduce the electroconductibility in the side gap, protecting the machined blade side. Therefore, the lateral-flow sleeve machining blade was less affected by stray corrosion, the blade surface quality was better, and the surface pitting was not obvious, as shown in Figure 11(c).

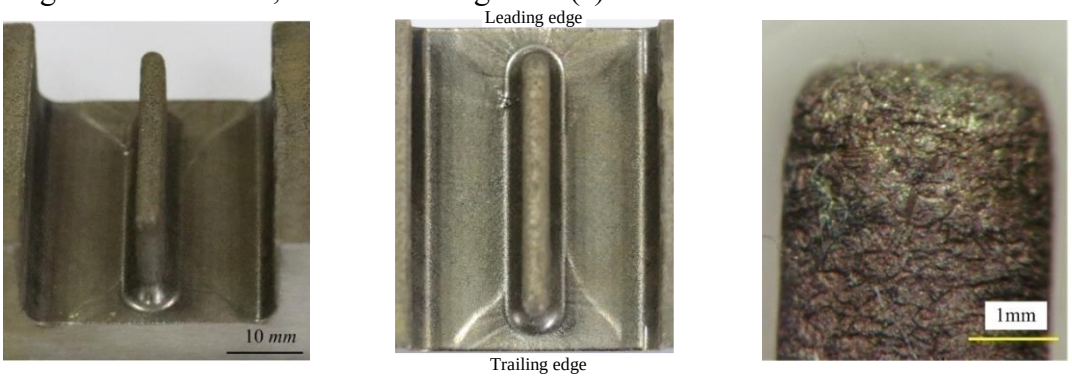

(a) Whole shape of blade (b) Blade hub (c) Enlarged view of blade tip

Figure 11. Blade machined by the forward flow mode of electrochemical trepanning

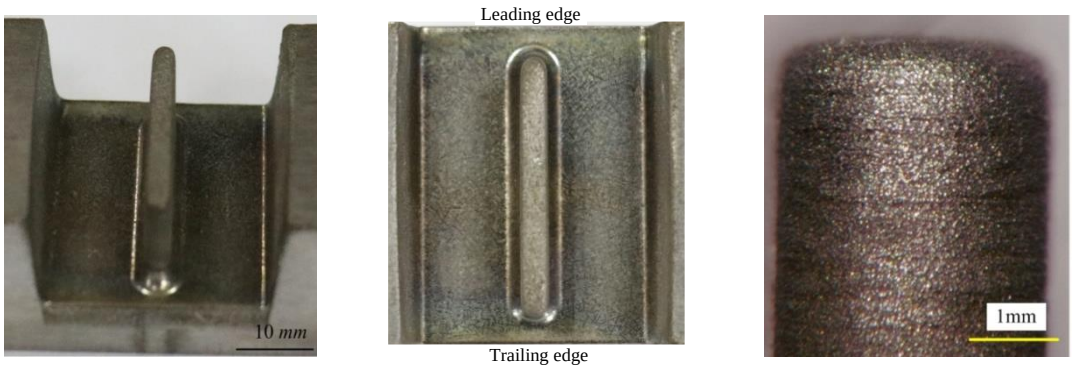

(a) Whole shape of blade (b) Blade hub (c) Enlarged view of blade tip

Figure 12. Blade machined by the lateral flow mode of electrochemical trepanning

In order to quantitatively analyze the surface quality of the machined blade, the roughness of the sample was detected by the roughness detector. When the feeding rate was the same (2 mm/min), the roughnesses of the lateral-flow and forward-flow sleeve processing were 1.581 μm and 2.327 μm, respectively; the blade-roughness detection results are shown in Figure 13. The results showed that in lateral flow, the electrolyte flowrate in the side gap was reduced, which had a significant effect on improving the blade roughness. In addition, compared with the experimental results of other papers, the experiment in this paper can obtain better surface quality. For example, under the condition of 2mm/min, the surface roughness obtained by Zhu is about 2.5 μm[15]. This is obviously higher than the

experimental results in this paper of about 1.581 μm, which may be due to the more complex flow field caused by the curved blade structure in Zhu's experiments.

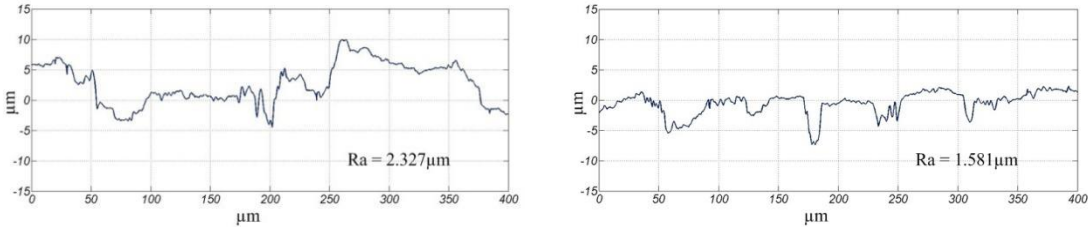

(a) Forward flow (b) Lateral flow

Figure 13. Comparison of the machined surface roughness.

4.4. Comparison of machining accuracy of machined samples

In trepanning ECM, the deviations of the top and bottom of the machined sample are different. In other words, there is a taper angle in the processed sample, as shown in Figure 14. In this study, the taper angle was selected to analyze the machining accuracy under different flow fields:

$$\alpha = \tan^{-1}\left(\frac{d_B - d_T}{H}\right). \quad (4)$$

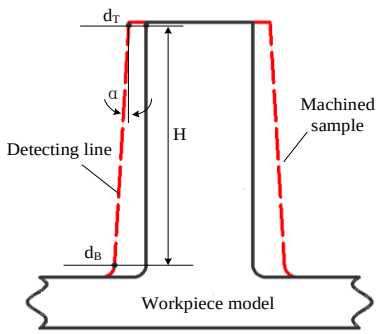

Figure 14. Schematic graph of the taper of the machined blade.

The contour of the detection line on the processed sample was measured by using a three-coordinate detector under different feed speeds, and then the cone angle was calculated according to Equation (4). The results are shown in Figure 15. It can be seen that with the increase of feeding rate, the corrosion time of the stray current on the blade side decreased, and the taper of the blade machined by the two flow modes decreased gradually. This is similar to the experimental results of Xu[16] and Hu[17]. When the feeding rate reached more than 2 mm/min, the taper of the blade machined by the two methods could be controlled within 0.04 mm/7 mm. According to Equation (4), the taper angle of machined blade can be calculated to be about 0.327°. This is significantly less than Xu's experimental results of about 8.36° [16], which may be due to the lower feed rate used in Xu's experiment, resulting in greater stray corrosion on the side wall of the machined blade. It is worth noting that Hu achieved a better taper angle of machined blade by using gas film insulation in their experiments, and achieved a

nearly right-angled machining performance by optimizing the cathode air supply to reduce the stray corrosion of machined blade sidewall.

Under the same feeding rate, the blade taper of the lateral-flow machining was smaller than that of the forward-flow machining, especially when the machining speed was low. As such, the lateral-flow machining had obvious advantages in reducing the taper of the blade.

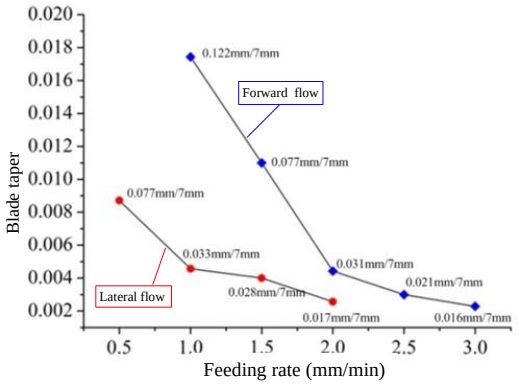

Figure 15. Comparison of blade taper between forward flow and lateral flow.

5. CONCLUSION

In electrochemical machining, the flow field is a key factor that affects machining stability, machining efficiency, and machining-surface quality. This paper focused on the study of flow-field characteristics in electrochemical sleeve machining. Through a series of simulations and experimental studies, the influence law of different flow-field modes on electrochemical sleeve machining was discussed, and the conclusions can be summarized as follows.

(1) Using ANSYS to carry out the simulation experiment of forward flow and lateral flow, the simulation results of the flow field show that, compared with forward flow, lateral flow has lower velocity but better uniformity.

(2) The fixtures of the two flow patterns are designed and manufactured. The experimental results show that compared with lateral flow, forward flow can obtain a higher feed speed.

(3) The comparison of the surface morphology of the machined samples under different flow-field modes shows that, compared with forward flow, lateral flow is more uniform and smoother, and the stray corrosion is effectively controlled, leading to a better surface quality.

(4) The comparison of the machining accuracy of the processed samples under different flow-field modes shows that, compared with forward flow, lateral flow can obtain a smaller taper angle, and when the feed speed is less than 2 mm/min, the machining-accuracy advantage of lateral flow is more obvious.

ACKNOWLEDGEMENTS
The authors wish to acknowledge the financial support provided by the Open Fund for Jiangsu Key Laboratory of Advanced Manufacturing Technology (HGAMTL-1903) .

References

1. W.Z. Zou, X. He, W.C. Zhang, Z.T. Niu, X.Q. Zheng, *J. Aerosp. Eng.,* 233 (14)(2019) 5380-5392.
2. L. Huang, Y. Cao, X.Y Zhang, J.H. Zhang, Y. Lei, Y. Li, Q.M. Fan, *Sci. Rep.,* 11 (2021) 12817.
3. K. Zhai, L. Tang, J. Liu, X.Y. Zhang, Y.N. Yan, X. Feng, *Int. J. Adv. Manuf. Technol.,* (2021).
4. K.P. Rajurkar, D. Zhu, J.A. McGeough, J. Kozak, D.A. Silva, *CIRP. Ann.,* 48 (2)(1999) 567-79.
5. Y.C. Ge, Z.W. Zhu, D.Y. Wang, *Electrochim. Acta.,* 253 (2017) 379-389.
6. Z.Y. Xu, Y.D. Wang, Chin J Aeronaut 34(2) (2021) 28–53.
7. J. Lin, D. Zhu, X. Hu, *Int. J. Adv. Manuf. Technol*., 112 (2021) 2533-2545.
8. Z.Y. Xu, L.Y. Sun, Y .Hu, J.C. Zhang, *Int. J. Adv. Manuf. Technol.,* 71 (1–4)(2014) 459-69.
9. X.L. Fang, N.S. Qu, T.D. Zhang, Z.Y. Xu, D. Zhu, *J. Mater. Process. Technol.,* 214 (1)(2014) 36-43.
10. L. Tang, W.M. Gan, *Int. J. Adv. Manuf. Technol.,* 72 (9–12)(2014) 1759-1766.
11. Y.C. Ge, Z.W. Zhu, Z. Ma, D.Y. Wang, *J. Mater. Process. Technol.*, 258 (2018) 89-96.
12. L. Dabrowski, T. Paczkowski, *Russ. J. Electrochem.,* 41 (1)(2005) 91-8.
13. A.N. Zaytsev, V.P. Zhitnikov, T.V. Kosarev, *J.* Mater. Process. Technol., 149 (1)(2004) 439-444.
14. Z.Z. Gu, D. Zhu, T.Y. Xue, A. Lin, D. Zhu, *Int, J. Adv. Manuf. Technol*., 89 (2017) 877–884.
15. D. Zhu, T.Y. Xue, X.Y. Hu, Z.Z. Gu, *Chinese, J, Aeronaut.,*32(2019):1748-1755.
16. J.W. Xu, D. Zhu, J.H. Lin, J.H. Lin, X.Y. Hu, *Int. J. Adv. Manuf. Technol.,* 107 (2020) 1551-1558.
17. X.Y. Hu, D. Zhu, J.B. Li, Z.Z. Gu, *J. Mater. Process. Technol.*, 267(2019) 247-256.